

Gravity currents over mobile sediment beds

By A. D. Leonelli[†], E. Meiburg[‡], S. Balachandar[‡], J. Wang and P. Johnson[¶]

We conduct direct numerical simulations of turbidity currents propagating over fully resolved, erodible sediment beds. To address the wide range of grain sizes in turbidity currents—from mud, $\mathcal{O}(10\ \mu\text{m})$, to sand, $\mathcal{O}(1\ \text{mm})$, or larger—we employ a two-level modeling approach in which the larger sand grains that constitute the bed are resolved with the immersed boundary method and an Eulerian framework is used to model the finer suspended sediment. We conduct lock exchange simulations using four classes of substrate and sediment mobility: smooth wall, fixed bed, bed load transport, and suspended load transport. The reported front location and velocity demonstrate that the presence of a bed retards the current relative to the smooth wall case, with full resuspension of the substrate resulting in the slowest propagating current. Streamwise velocity and turbulent kinetic energy profiles taken within the current show that erosion, and the resultant increase in bed porosity, enhances the vertical mixing of mass and momentum. Finally, we demonstrate a nonmonotonic increase in basal friction as a function of bed mobility.

1. Introduction

Turbidity currents are sediment-laden gravity currents that propagate along the seafloor, driven by the action of gravity on the density difference between the sediment suspension and the clear, ambient fluid. As they travel, turbidity currents continuously erode and deposit sediment, with turbulence acting to keep the sediment in suspension. When the turbulence produced in the current is strong enough to sustain the suspension, the current is termed auto-suspending. Such currents can reach immense scales, with a single event transporting up to $\mathcal{O}(100\ \text{km}^3)$ of sediment and traveling in excess of $\mathcal{O}(1,000\ \text{km})$. Turbidity currents are believed to be the primary mechanism of sediment transport from the coast to the deep ocean and therefore play a critical role in the global sediment cycle and the formation of deep-sea hydrocarbon reservoirs and mineral deposits (Meiburg & Kneller 2010). Additionally, they pose a severe risk to submarine infrastructure such as pipelines, wellheads and telecommunication cables (Carter *et al.* 2014).

Due to the unpredictability and destructive nature of turbidity currents, field observations of turbidity currents are difficult to conduct. As a result, the majority of our knowledge on turbidity currents is derived from comparatively small laboratory-scale experiments and simplified numerical simulations (Meiburg & Kneller 2010). Motivated by the inexplicable distances turbidity currents travel, recent focus has been placed on the interaction between the current and its boundaries. Detailed laboratory and numerical studies have considered the flow of gravity currents over smooth, horizontal walls (Huppert & Simpson 1980; Necker *et al.* 2002; Shin *et al.* 2004; Cantero *et al.* 2017), resulting in the identification of several stages of flow. First, the current exhibits a slumping phase,

[†] Department of Mechanical Engineering, University of California, Santa Barbara

[‡] Department of Mechanical and Aerospace Engineering, University of Florida

[¶] Department of Mechanical and Aerospace Engineering, University of California, Irvine

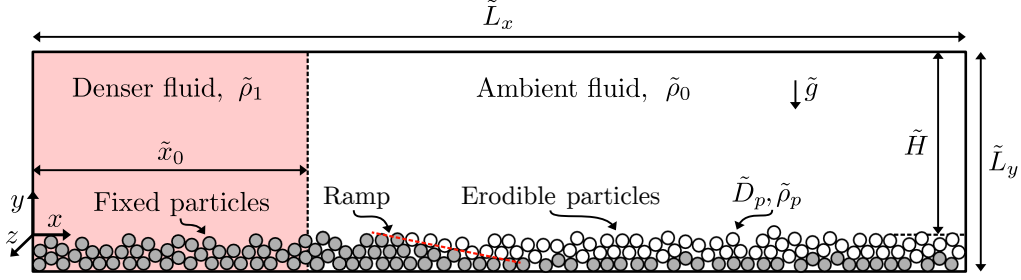


FIGURE 1. Schematic of the lock exchange configuration used in this study (not to scale). The dashed red line denotes the ramp used to partition fixed and erodible particles so that the formation of a step is avoided. The bed height, displayed as a black dashed line, is used to define the free depth, \tilde{H} , and serves as the y -origin of the coordinate axes.

characterized by a constant front velocity. Next, the current may enter an inertial phase, where inertial forces balance buoyant forces. The final stage is a viscous phase, where viscous effects become significant and the current slows and eventually dissipates. Due to scale or resource constraints, many studies, including this work, consider only the slumping phase. Recent studies have evaluated the effect of macroscopic roughness and obstacles on current propagation and structure (Tokyay *et al.* 2011; Cenedese *et al.* 2018; Jiang & Liu 2018). Zhou *et al.* (2017) investigated slumping gravity currents over an array of cylinders and demonstrated two flow regimes controlled by the cylinder packing: one where the current flows through the cylinder array for larger periodic spacings and, at closer packings, a regime where the current flows over the top. Köllner *et al.* (2020) present particle-resolved direct numerical simulations of gravity currents over fixed beds of closely packed spherical particles with which they demonstrate that the bottom friction is strongly dependent on particle size but weakly dependent on the depth of the bed. Finally, experimental studies that consider mobile sediment beds report a clear connection between erosion and current structure, though the micro-mechanical mechanisms responsible for the changes remain unclear (Zordan *et al.* 2018).

In this work, we investigate the propagation of gravity currents over randomly packed beds of erodible particles. The erodibility of the sediment bed is controlled by the particle density and allows for the consideration of three erosive behaviors: no transport [fixed bed (FB)]; bed load transport (BL), characterized by particles skipping along the top layer; and suspended load transport (SL), in which the coarser sediment is fully brought into suspension. An additional current propagating over a smooth wall (SW) is also used for comparison.

2. Physical description

We consider a domain of size $\tilde{L}_x \times \tilde{L}_y \times \tilde{L}_z = 15.625\tilde{H} \times 1.25\tilde{H} \times 0.25\tilde{H}$, where the free depth, $\tilde{H} = \tilde{L}_y - \tilde{\eta}$, is taken as the characteristic length scale and $\tilde{\cdot}$ indicates a dimensional quantity. The channel is initially partitioned into two regions along the streamwise, x , direction; the left lock region, $\tilde{x}_0 = 6.25\tilde{H}$, is filled with a dilute suspension of fine sediment (e.g., mud) with an effective density, $\tilde{\rho}_1$, while to the right of the lock is an ambient fluid (e.g., water), density $\tilde{\rho}_0$. The density difference, $\Delta\rho = (\tilde{\rho}_1 - \tilde{\rho}_0) / \tilde{\rho}_0 = 0.01$, is small so that the Boussinesq approximation may be taken. Both fluids are assumed incompressible and Newtonian with viscosity $\tilde{\nu}$. Gravity, \tilde{g} , acts in the vertical direction.

At the bottom of the domain is a sediment bed constituted of spherical particles of diameter $\tilde{D}_p = 0.125\tilde{H}$ and density, $\tilde{\rho}_p$. In this study, the relative density between the sediment and ambient fluid, $\rho_s = \tilde{\rho}_p/\tilde{\rho}_0$, is used to control the erodibility of the bed. Due to the reduced flow scales and shear stress, ρ_s must be small to allow for erosion.

The bottom layers of the bed—particles with center of mass $\tilde{y}_i < 0.6\tilde{D}_p$ —are glued in place to provide roughness. The particles in the lock are also held fixed. To avoid forming a step, a ramp of length $1.25\tilde{H}$ is used to define the fixed-erodible interface between the total bed height, $\tilde{\eta}$, and the bottom roughness layer. Lastly, the bed height, $\tilde{\eta}$, is measured according to the following threshold based on the volume fraction of coarse particles, $\tilde{\eta} = \max(\tilde{y}|\langle\phi\rangle_{x,z} = 0.01) = 0.25\tilde{H}$. Hereafter, unless otherwise specified, the origin is located at the left wall in x and the bed height in y , such that $\tilde{\eta} = 0$ and the domain spans $\tilde{y} \in [-0.25\tilde{H}, \tilde{H}]$. A schematic is presented in Figure 1.

3. Methodology

We consider the Navier-Stokes Boussinesq equations for an incompressible, Newtonian fluid,

$$\partial_t \mathbf{u} + \mathbf{u} \cdot \nabla \mathbf{u} = -\nabla p + Re^{-1} \nabla^2 \mathbf{u} + Ri \mathbf{e}_y \xi_f c + \mathbf{f}, \quad (3.1)$$

and continuity,

$$\nabla \cdot \mathbf{u} = 0, \quad (3.2)$$

where the equations are made dimensionless using the free depth, \tilde{H} , characteristic velocity, $\tilde{U} = \sqrt{\tilde{g}'\tilde{H}}$, where $\tilde{g}' = \tilde{g}\Delta\rho$ is the reduced gravity, and characteristic pressure, $\tilde{P} = \tilde{\rho}_0\tilde{U}^2$. Since the current is observed to primarily flow over the bed, the Reynolds number, $Re = \tilde{U}\tilde{H}/\tilde{\nu}$, is constructed using the free depth. Of particular importance is the buoyancy term, in which the Richardson number, $Ri = \tilde{H}\tilde{g}'/\tilde{U}^2 = 1$, is introduced to express the ratio of buoyancy to flow shear. Additionally, $c(\mathbf{x}, t)$ is the concentration of denser fluid used to model the fine sediment suspension and $\xi_f(\mathbf{x}, t)$ is the fluid indicator function, which takes a value of unity in the volume occupied by fluid or zero inside a particle. The effective density of the fluid, ρ , is modeled using the concentration field, $c(\mathbf{x}, t)$, and is formulated as

$$\rho = 1 + \Delta\rho c. \quad (3.3)$$

The concentration field obeys the transport equation,

$$\partial_t c + (\hat{\mathbf{u}} - v_s \mathbf{e}_y) \cdot \nabla c = Pe_L^{-1} \nabla \cdot \xi_f \nabla c, \quad (3.4)$$

where the Peclet number expresses the ratio of concentration advection to diffusion, $Pe = \tilde{U}\tilde{H}/\tilde{\kappa}$, and $\tilde{\kappa}$ is the diffusivity of the fine particulate suspension. The Schmidt number, $Sc = Pe/Re = \tilde{\nu}/\tilde{\kappa}$, can also be formulated and expresses the ratio of diffusivities of the fine sediment suspension to fluid momentum. In this study, the settling velocity of the suspension is set to zero, $v_s = 0$. Finally, since the particle velocity is not reflected in the velocity field of the immersed boundary method (IBM), Eq. (3.4) uses the compound velocity, $\hat{\mathbf{u}} = \xi_f \mathbf{u} + (1 - \xi_f) \mathbf{u}_c$, where \mathbf{u}_c is the solid-body velocity field computed within each particle.

Equations (3.1), (3.2), and (3.4) are solved over the entire computational domain. The IBM is used to resolve the coarse bed particles and works to enforce the no-slip condition on the particle surfaces. The bottom and left walls are also treated as no-slip boundaries, while the right and top walls are maintained as impermeable, stress-free surfaces, as do-

Name	$L_x \times L_y \times L_z$	$N_x \times N_y \times N_z$	D_p	$D_p/\Delta x$	ρ_s	n_p	Re	Pe	Erodible
SW	$15.625 \times 1 \times 0.25$	$4500 \times 288 \times 72$	—	—	—	0	5603	56030	—
FB	$15.625 \times 1.25 \times 0.25$	$4500 \times 360 \times 72$	0.125	36	—	1392	5603	56030	N
BL	$15.625 \times 1.25 \times 0.25$	$4500 \times 360 \times 72$	0.125	36	1.01	1392	5603	11206	Y
SL	$15.625 \times 1.25 \times 0.25$	$4500 \times 360 \times 72$	0.125	36	1.05	1392	5603	11206	Y

TABLE 1. Parameters for the four simulations considered: smooth wall (SW), fixed bed (FB), bed load transport (BL), and suspended load transport (SL). Details on the cubic grid and resolution per particle diameter are also provided.

ing so better mimics the longer free-surface lock exchange configurations often used in experimental works. The transverse direction is made periodic. The concentration field is modeled using the volume of fluid method. Each wall—left, right, top, and bottom—is made impermeable to the concentration field. Finally, the particles are indirectly made impenetrable through the combined effect of the particle indicator function and compound velocity in the diffusive and advective terms of Eq. (3.4), respectively. The implementation of the IBM-based particle-resolved direct numerical simulation used in this study is described in detail by Biegert *et al.* (2017). The coupling to the concentration field is further elaborated by Ardekani *et al.* (2018).

3.1. Simulation parameters

We conduct four simulations of gravity currents produced by lock exchange and investigate the effect of substrate roughness, porosity, and erosion on current properties. Three cases explore the erodibility of the immersed sediment bed by varying ρ_s . In doing so, three transport modes FB, BL, and SL are observed for the coarse grains. A fourth simulation is conducted with a SW. Since the currents are observed to travel over the sediment bed, the domain height for the SW case is reduced to the free depth, $H = 1$. To construct the bed for the three cases with resolved particles, $n_p = 1392$ particles are randomly distributed throughout the domain and allowed to settle in a precursor simulation. This results in a bed of height $\eta = 0.25$. The particle diameter, $D_p = 0.125$, is chosen so that resolving the pore spaces in the bed remains computationally tractable using the cubic grid required by the IBM. The Reynolds number, $Re = 5603$, is chosen to be the maximal value so that the smallest scales of the resultant turbulent flow are resolved. Schmidt numbers are chosen in accordance to the findings of Bonometti & Balachandar (2008) and Necker *et al.* (2005), who demonstrated that the Schmidt number—the ratio of kinematic viscosity to the diffusivity of the fine suspension—has a weak influence on the dynamics of gravity currents for $Sc > 1$ and $Re \geq \mathcal{O}(10^4)$. Thus, $Sc = \{2, 10\}$ are selected. A summary of simulation parameters is presented in Table 1.

At time $t = 0$ the lock is released and the system is allowed to relax under gravity. This results in a mutual intrusion flow in which the denser fluid propagates to the right over the sediment bed.

4. Results

4.1. Overview

The time evolution of concentration for the BL case is presented in Figure 2 as five panels advancing in time from top to bottom. The upper panel displays the initial state, where

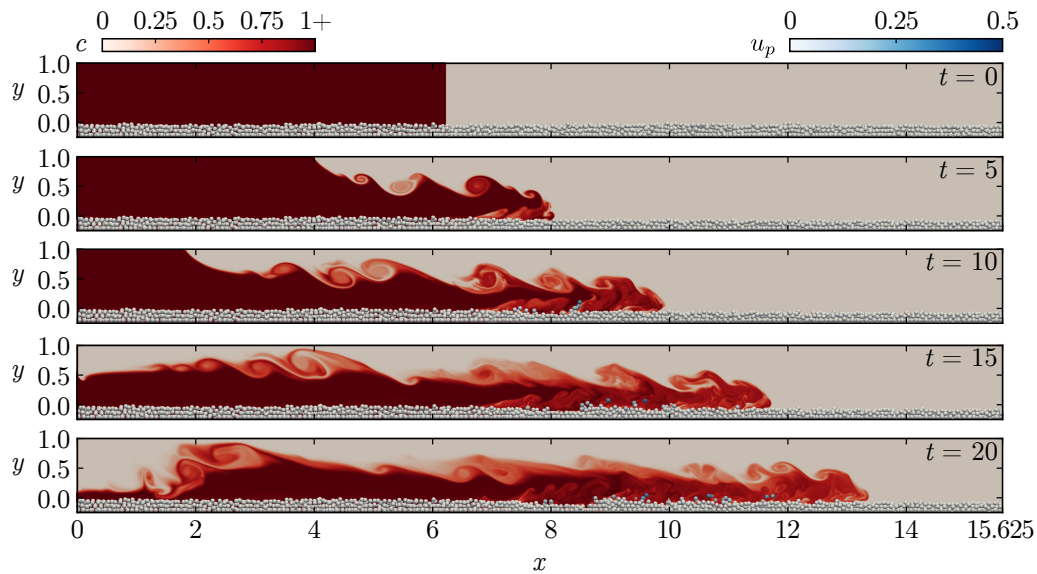


FIGURE 2. Temporal evolution of a concentration field slice for the case demonstrating bed load transport (BL). A side view of the 3D-rendered bed of resolved particles is overlaid onto the concentration field slice. In the bed, particles are colored by their velocity magnitude. Videos for each case can be found here: SW, FB, BL, SL.

we see that the fine sediment suspension, colored red, is entirely located in the lock region. After release, $t > 0$, a mutual intrusion flow is created with the denser suspension of fine sediment traveling rightward, over the bed of coarser grains. Above the dense current, a counterflow of the ambient fluid enters the lock along the upper surface of the domain. Shortly after release, prominent Kelvin-Helmholtz rollers indicative of a shear instability develop along the interface between the suspension and ambient. After some time, $t \approx 15$, the lock is drained and the front is expected to eventually slow until the current dissipates due to viscous effects. Observations are made until the distance between the current front and the right wall of the domain becomes less than the domain height, at which point the horizontal confinement can no longer be ignored. Also observable in the sequence of panels is the erosion of the coarse particles by the passing gravity current. A side view of the 3D bed, in which particles are colored by their velocity magnitude, is superimposed onto the concentration field slice. In the panels for $t = 15$ and $t = 20$, the current can be observed eroding the top layer of particles.

A comparison of span-averaged concentration profiles across the four simulations is shown in Figure 3. Since there is no concentration in the particles, their location can be seen in the three simulations initialized with resolved beds. It is clear from visual inspection that the front location of the SW case is ahead while differences in the other three cases are discussed in more detail in Section 4.3. Also noteworthy is the lighter color of the current and penetration of concentration into the bed in the FB, BL, and SL cases. This is indicative of the exchange of fluid between the current and bed, which leads to a loss of buoyancy and expected slowdown of the current. Finally, the SL case exhibits an unexpected behavior with the presence of what seems to be two fronts: the current front at $x \approx 7$ and an internal front at $x \approx 5$, marked by the absence of coarse particles.

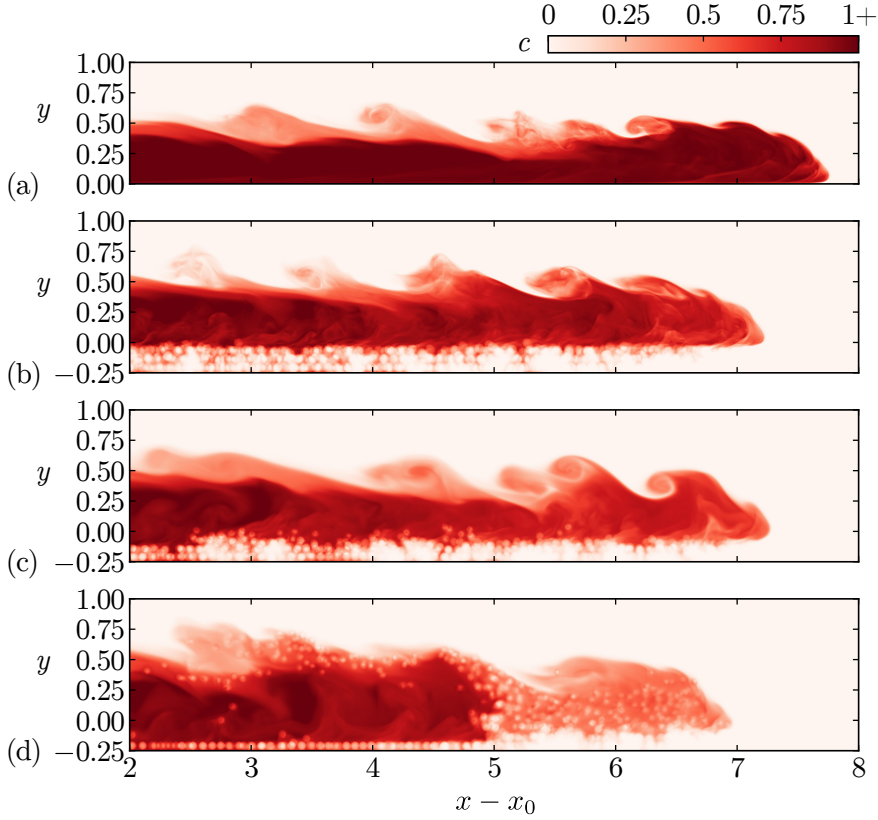


FIGURE 3. Span-averaged concentration profiles at $t = 15.6$ for each case: (a) smooth wall (SW), (b) fixed bed (FB), (c) bed load transport (BL), and (d) suspended load transport (SL). The volume within particles is void of concentration such that particles appear as lighter patches in the span-averaged fields.

In the region between the $x = 5$ and $x = 7$ fronts, the current is laden with resolved particles that get eroded and transported up to the interface. Whether this behavior is an artifact of the shallow nature of the bed is unclear and a topic of further interest as we develop larger-scale simulations with smaller particles and deeper beds.

4.2. Metrics

In this work, the interface between the current and ambient is determined using the buoyant height (Shin *et al.* 2004),

$$h(x, t) = \int_0^1 \langle c \rangle_z dy, \quad (4.1)$$

where $\langle \cdot \rangle_z$ indicates a spanwise average. The front location, $x_F(t)$, is defined as the maximum value of x , where $h(x, t) = 0.125$,

$$x_F(t) = \max \{x \mid h(x, t) = 0.125\}. \quad (4.2)$$

The specific value of h is chosen to be consistent with the experimental procedures of Köllner *et al.* (2020) and allows for comparison of the FB case. It follows that the front

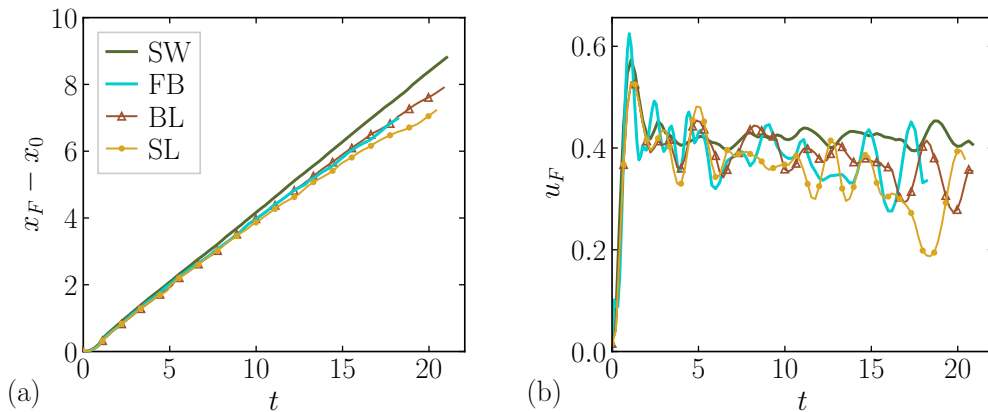


FIGURE 4. The front positions (a) and velocities (b) over time as computed by Eqs. (4.2) and (4.3), respectively. The positions, velocities, and times are scaled using the free depth, H , which allows for a collapse of the data at early times when the currents mainly propagate over the beds.

speed, $u_F(t)$, is given as,

$$u_F(t) = \dot{x}_F(t). \quad (4.3)$$

4.3. Front kinematics

The front location and front velocity over time are presented in Figure 4. The SW case is seen to advance with a constant front speed, as expected during the initial slumping stage. The currents with beds appear to slow relative to the SW case. This is likely due to drainage and the subsequent loss of buoyancy as the current exchanges fluid with the pore spaces in the bed. It is apparent that the front speed of the SL case is further reduced. This may suggest that the combined effect of the entrainment of ambient fluid from within the bed and the work done by the fluid to erode coarser grains outweighs the effective increase in current buoyancy due to the higher density of the particle. Section 4.5 clarifies the sources of drag, though more detailed analysis of the momentum balance and energy budget is required.

4.4. Velocity and turbulent kinetic energy profiles

The velocity field is probed over a plane following behind the current front at a distance $x_{\text{sample}}(t) = x_F(t) - 2$. Approximately 60 snapshots are span and time averaged over a window beginning at $t = 10$ and ending when $L_y - x_F(t) \leq 1$. The resultant streamwise velocity, U , and turbulent kinetic energy, $k = \langle u'_i u'_i \rangle_z / 2$, profiles are presented in Figure 5(a, b). In both panels, the profiles for the SW case, which has a shorter domain in y , are aligned to the other cases by the top wall.

Each streamwise velocity profile displays three distinct regions: little to no flow within the bed or near the wall; a parabola-like profile within the rightward-propagating gravity current $0 < y < 0.5$; and, above $y \approx 0.5$, a left-moving plug-like counterflow. In the initial bed region, $y < 0$, it is clear that both the introduction of porosity—FB—and the erosion of the bed—BL and SL—result in a deeper current and reduction of maximum streamwise velocity. The counterflow, $y > 0.5$, is relatively unchanged despite the differences in the bed region, $y < 0$. Also worth investigating further is the nose-like structure observed in the streamwise velocity profile of the FB case.

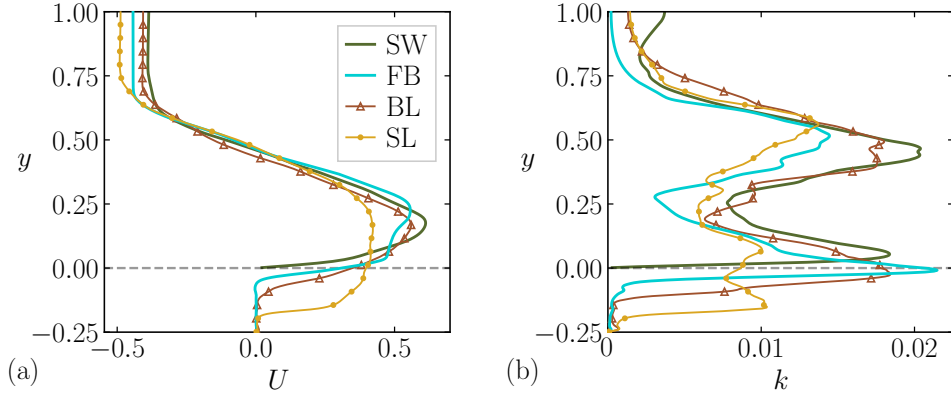


FIGURE 5. Span- and time-averaged streamwise velocity (a) and turbulent kinetic energy (b) profiles. Averages are taken at a fixed distance behind the rightward-propagating front of the gravity current, $x_{\text{sample}}(t) = x_F(t) - 2$. The profiles for the smooth wall (SW) case are shifted upward by a distance of 0.25 so that the top walls of the domains are aligned. The top of the initial bed, $y = 0$, is also displayed as a gray dashed line.

Turbulence is driven in the current by the interaction between the bottom boundary—bed or wall—and the shear-layer at the interface between the dense gravity current and the counterflow. To quantify the intensity and location of the turbulence, the vertical profiles of turbulent kinetic energy (t.k.e) are presented in Figure 5(b). Each profile generally exhibits two expected peaks: one above the bottom boundary—bed or wall—and another in the shear-layer at the interface between current and counterflow. Similar to the streamwise velocity profiles, the t.k.e. is observed to penetrate deeper into the bed due to porosity and the removal of particles by erosion. There is a significant difference between the SL case and the others, with the near-bed peak being much less prominent and more homogeneous across a larger region. Finally, the noise in the profiles suggests that the statistics are likely not yet converged.

4.5. Basal friction

To quantify the effect of basal drag, we consider the friction coefficient,

$$C_f(x, z, t) = -\frac{vu - Re^{-1}\partial_y u}{u_F^2/2}. \quad (4.4)$$

Equation (4.4) is computed at $x_{\text{sample}}(t) = x_F(t) - 2$, height y_{C_f} , and averaged over time in the same manner as the profiles in Section 4.4. For the FB, BL, and SL cases, y_{C_f} is taken as the bed height after erosion, whereas for the SW case, y_{C_f} corresponds to the bottom wall. The resultant friction coefficients and the individual advective and diffusive contributions are reported in Table 2. The values for the SW and FB cases are in good agreement with those reported by Köllner *et al.* (2020) for the flow over a smooth wall and hexagonally packed bed, respectively. Interestingly, the friction coefficient increases nonmonotonically with bed mobility. It appears that this is a result of the interplay between the increased advective momentum transport due to porosity and erosion and the decreased shear stress due to enhanced vertical mixing. Note that the contribution of the mobile particles to Eq. (4.4) is missing and, once included, will alter the reported values for the BL and SL cases.

Name	y_{C_f}	$\langle C_f \rangle$	$\langle vu / (u_F^2/2) \rangle$	$\langle -Re^{-1} \partial_y u / (u_F^2/2) \rangle$
SW	0	$2.8 \cdot 10^{-2}$	0	$2.8 \cdot 10^{-2}$
FB	0	$8.9 \cdot 10^{-2}$	$6.9 \cdot 10^{-2}$	$2.0 \cdot 10^{-2}$
BL	0	$8.1 \cdot 10^{-2}$	$7.1 \cdot 10^{-2}$	$1.0 \cdot 10^{-2}$
SL	-0.12	$10.2 \cdot 10^{-2}$	$10.0 \cdot 10^{-2}$	$0.3 \cdot 10^{-2}$

TABLE 2. Span- and time-averaged bottom friction coefficients for each simulation. Eq. (4.4) is computed following the front at $x_{\text{sample}}(t) = x_F(t) - 2$ at height, y_{C_f} . For the fixed bed (FB), bed load (BL), and suspended load (SL) cases y_{C_f} is the measured bed height after erosion whereas for the smooth wall (SW) case, y_{C_f} corresponds to the bottom wall. Also reported are the individual contributions of advective and the diffusive momentum transport to the C_f . Note that the values for the BL and SL cases will change after the contribution of the eroded particles is added to the stress balance.

5. Conclusions and outlook

This report presents a two-level modeling approach for simulating turbidity currents propagating over erodible substrates. Here, fine grains are modeled as a continuum while the coarser sediment bed is resolved with the IBM. Four direct numerical simulations are conducted: Three explore the propagation of a gravity current over a bed of particles with varying levels of erodibility, controlled by particle density, while a final simulation considers a smooth base. The presence of a bed is shown to retard the current relative to the SW case. Full resuspension of the bed results in the slowest propagating current. Streamwise velocity and t.k.e. profiles taken at a fixed distance from the front are presented for each case. It is observed that bed erosion allows for flow to penetrate lower in the domain as particles are removed and the porosity of the bed region increases. The t.k.e. presents two expected peaks: one at the shear-layer between dense gravity current and counterflow and another near the bed or wall where the no-slip condition is enforced. Suspension of particles appears to flatten the t.k.e. profile. Lastly, a friction coefficient is computed to quantify basal drag. It is found that increased erosion results in a non-monotonic increase in bottom friction. The nonmonotonic nature of the increase appears to be due to changes in the relative contributions of advective and diffusive momentum transport through the base of the current, though the contribution of the mobile particles to the momentum balance is lacking.

The simulations reported here build confidence in the two-level approach, and future simulations using the same framework can address the following: (i) smaller particles to smooth out the discrete nature of erosion events, (ii) a deeper bed such that highly erosive currents do not exhaust the supply of coarse particles, and (iii) a non-zero settling velocity for the fine sediment modeled by the concentration field. Furthermore, future work includes analysis of the coarse particle contribution to the friction coefficient as well as a detailed study of the energy budget.

Acknowledgments

The authors thank A. Ooi and W. Lu for the insightful discussions. The authors acknowledge use of computational resources from the Yellowstone and Armstrong clusters awarded by the National Science Foundation to CTR.

REFERENCES

- ARDEKANI, N. M., ABOUALI, O., PICANO, F. & BRANDT, L. 2018 Heat transfer in laminar Couette flow laden with rigid spherical particles. *J. Fluid Mech.* **834**, 308–334.
- BIEGERT, E., VOWINCKEL, B. & MEIBURG, E. 2017 A collision model for grain-resolving simulations of flows over dense, mobile, polydisperse granular sediment beds. *J. Comput. Phys.* **340**, 105–127.
- BONOMETTI, T. & BALACHANDAR, S. 2008 Effect of Schmidt number on the structure and propagation of density currents. *Theor. Comput. Fluid Dyn.* **22**, 341–361.
- CANTERO, M. I., BALACHANDAR, S. & GARCIA, M. H. 2007 High-resolution simulations of cylindrical density currents. *J. Fluid Mech.* **590**, 437–469.
- CARTER, L., GAVEY, R., TALLING, P. & LIU, J. 2014 Insights into submarine geohazards from breaks in subsea telecommunication cables. *Oceanog.* **27**, 58–67.
- CENEDESE, C., NOKES, R. & HYATT, J. 2018 Lock-exchange gravity currents over rough bottoms. *Environ. Fluid Mech.* **18**, 59–73.
- HUPPERT, H. E. & SIMPSON, J. E. 1980 The slumping of gravity currents. *J. Fluid Mech.* **99**, 785–799.
- JIANG, Y. & LIU, X. 2018 Experimental and numerical investigation of density current over macro-roughness. *Environ. Fluid Mech.* **18**, 97–116.
- KÖLLNER, T., MEREDITH, A., NOKES, R. & MEIBURG, E. 2020 Gravity currents over fixed beds of monodisperse spheres. *J. Fluid Mech.* **901**, A32.
- MEIBURG, E. & KNELLER, B. 2010 Turbidity currents and their deposits. *Annu. Rev. Fluid Mech.* **42**, 135–156.
- NECKER, F., HÄRTEL, C., KLEISER, L. & MEIBURG, E. 2002 High-resolution simulations of particle-driven gravity currents. *Int. J. Multiphas. Flow* **28**, 279–300.
- NECKER, F., HÄRTEL, C., KLEISER, L. & MEIBURG, E. 2005 Mixing and dissipation in particle-driven gravity currents. *Int. J. Multiphas. Flow* **545**, 339–372.
- PARKER, G., GARCIA, M., FUKUSHIMA, Y. & YU, W. 1987 Experiments on turbidity currents over an erodible bed. *J. Hydraul. Res.* **25**, 123–147.
- SHIN, J. O., DALZIEL, S. B. & LINDEN, P. F. 2004 Gravity currents produced by lock exchange. *J. Fluid Mech.* **521**, 1–34.
- TOKYAY, T., CONSTANTINESCU, G. & MEIBURG, E. 2011 Lock-exchange gravity currents with a high volume of release propagating over a periodic array of obstacles. *J. Fluid Mech.* **672**, 570–605.
- ZHOU, J., CENEDESE, C., WILLIAMS, T., BALL, M., VENAYAGAMOORTHY, S. K. & NOKES, R. I. 2017 On the propagation of gravity currents over and through a submerged array of circular cylinders. *J. Fluid Mech.* **831**, 394–417.
- ZORDAN, J., JUEZ, C., SCHLEISS, S. J. & FRANCA, M. J. 2018 Entrainment, transport and deposition of sediment by saline gravity currents. *Adv. Water Resour.* **115**, 17–32.